arXiv:1011.1255v1 [astro-ph.CO] 4 Nov 2010

The Detection of a Population of Submillimeter−Bright, Strongly-Lensed Galaxies

Mattia Negrello[1*], R. Hopwood[1], G. De Zotti[2,3], A. Cooray[4], A. Verma[5],
J. Bock[6,7], D. T. Frayer[8], M. A. Gurwell[9], A. Omont[10], R. Neri[11],
H. Dannerbauer[12], L. L. Leeuw[13,14], E. Barton[4], J. Cooke[4,7], S. Kim[4],
E. da Cunha[15], G. Rodighiero[16], P. Cox[11], D. G. Bonfield[17], M. J. Jarvis[17],
S. Serjeant[1], R. J. Ivison[18,19], S. Dye[20], I. Aretxaga[21], D. H. Hughes[21], E. Ibar[18],
F. Bertoldi[22], I. Valtchanov[23], S. Eales[20], L. Dunne[24], S. P. Driver[25],
R. Auld[20], S. Buttiglione[2], A. Cava[26,27], C. A. Grady[28,29],
D. L. Clements[30], A. Dariush[20], J. Fritz[31], D. Hill[25],
J. B. Hornbeck[32], L. Kelvin[25], G. Lagache[33,34], M. Lopez-Caniego[35],
J. Gonzalez-Nuevo[3], S. Maddox[24], E. Pascale[20], M. Pohlen[20], E. E. Rigby[24],
A. Robotham[25], C. Simpson[36], D. J. B. Smith[24], P. Temi[37], M. A. Thompson[17],
B. E. Woodgate[38], D. G. York[39], J. E. Aguirre[40], A. Beelen[34], A. Blain[7],
A. J. Baker[41], M. Birkinshaw[42], R. Blundell[9], C. M. Bradford[6,7], D. Burgarella[43],
L. Danese[3], J. S. Dunlop[18], S. Fleuren[44], J. Glenn[45], A. I. Harris[46],
J. Kamenetzky[45], R. E. Lupu[40], R. J. Maddalena[8], B. F. Madore[47],
P. R. Maloney[45], H. Matsuhara[48], M. J. Michałowski[19], E. J. Murphy[49],
B. J. Naylor[6], H. Nguyen[6], C. Popescu[50], S. Rawlings[5],
D. Rigopoulou[5,51], D. Scott[52], K. S. Scott[40], M. Seibert[47], I. Smail[53],
R. J. Tuffs[54], J. D. Vieira[7], P. P. van der Werf[19,55], J. Zmuidzinas[6,7]

[1]Department of Physics and Astronomy, The Open University, Walton Hall, Milton Keynes, MK7 6AA, UK
[2]Istitute Nazionale di Astrofisica (INAF), Osservatorio Astronomico di Padova, Vicolo Osservatorio 5, I-35122 Padova, Italy
[3]Scuola Internazionale Superiore di Studi Avanzati (SISSA), Via Bonomea 265, I-34136 Trieste, Italy
[4]Department of Physics and Astronomy, University of California, Irvine, CA 92697, USA
[5]Oxford Astrophysics, Denys Wilkinson Building, University of Oxford, Keble Road, Oxford,

OX1 3RH, uk

[6]Jet Propulsion Laboratory (JPL), Pasadena CA, 91009, USA

[7]California Institute of Technology, Pasadena, CA 91125, USA

[8]National Radio Astronomy Observatory Post Office Box 2, Green Bank, WV 24944, USA

[9]Harvard-Smithsonian Center for Astrophysics, Cambridge, MA 02138, USA

[10]Institut d'Astrophysique de Paris, Universitte Pierre et Marie Curie and CNRS, 98 bis boulevard Arago, 75014 Paris, France

[11]Institut de Radioastronomie Millimétrique (IRAM), 300 rue de la piscine, 38406 Saint-Martin d'Hères, France

[12]Laboratoire Astrophysique, Instrumentation et Modélisation Paris Saclay, Commissariat àl'Énergie Atomique (CEA)/Direction des Sciences de la Matière (DSM) - CNRS - Université Paris Diderot, Institut de recherche sur les lois fondamentales de l'Univers (Irfu)/Service d'Astrophysique, CEA Saclay, Orme des Merisiers, F-91191 Gif-sur-Yvette Cedex, France

[13] Physics Department, University of Johannesburg, Post Office Box 524, Auckland Park 2006, South Africa

[14]SETI Institute, 515 North Whisman Avenue Mountain View CA, 94043, USA

[15]Department of Physics, University of Crete, 71003 Heraklion, Greece

[16]Dipartimento di Astronomia, Universitá di Padova, Vicolo Osservatorio 2, I-35122 Padova, Italy

[17]Centre for Astrophysics Research, Science and Technology Research Institute, University of Hertfordshire, Herts AL10 9AB, UK

[18]UK Astronomy Technology Center, Royal Observatory Edinburgh, Edinburgh, EH9 3HJ, UK

[19] Scottish Universities Physics Alliance, Institute for Astronomy, University of Edinburgh, Royal Observatory,Edinburgh, EH9 3HJ, UK

[20]School of Physics and Astronomy, Cardiff University, The Parade, Cardiff, CF24 3AA, UK

[21]Instituto Nacional de Astrofísica, Óptica y Electrónica, Apartado Postal 51 y 216, 72000 Puebla, Mexico

[22]Argelander Institut fur Astronomie, Universit Bonn, Auf dem Hügel 71, 53121 Bonn, Germany

[23]Herschel Science Centre, European Space Astronomy Centre, European Space Agency (ESA), Post Office Box 78, 28691 Villanueva de la Cañada, Madrid, Spain

[24]School of Physics and Astronomy, University of Nottingham, University Park, Nottingham NG7 2RD, UK

[25]Scottish Universities Physics Alliance, School of Physics and Astronomy, University of St. Andrews, North Haugh, St. Andrews, KY16 9SS, UK

[26]Instituto de Astrofísica de Canarias, C/Vía Láctea s/n, E-38200 La Laguna, Spain

[27]Departamento de Astrofísica, Universidad de La Laguna (ULL), E-38205 La Laguna, Tenerife, Spain

[28]Eureka Scientific, 2452 Delmer Street, Suite 100, Oakland CA 94602, USA

[29]Goddard Space Flight Center, Code 667, Greenbelt Road, Greenbelt, MD 20771, USA

[30]Astrophysics Group, Physics Department, Blackett Lab, Imperial College London, Prince

Consort Road, London SW7 2AZ, UK

[31]Sterrenkundig Observatorium, Universiteit Gent, Krijgslaan 281 S9, B-9000 Gent, Belgium

[32]Department of Physics and Astronomy, University of Louisville, Louisville, KY 40292, USA

[33]Institut d'Astrophysique Spatiale (IAS), Bâtiment 121, F-91405 Orsay, France

[34]Université Paris-Sud 11 and CNRS (UMR 8617), 91400 Orsay, France

[35]Instituto de Fisica de Cantabria, Consejo Superior de Investigaciones Científicas - Universidad de Cantabria, Avenue de Los Castros s/n, Santander, 39005, Spain

[36]Astrophysics Research Institute, Liverpool John Moores University Twelve Quays House, Egerton Wharf, Birkenhead, CH41 1LD, UK

[37]Astrophysics Branch, NASA Ames Research Center, Mail Stop 245-6, Moffett Field, CA 94035, USA

[38]NASA Goddard Space Flight Center, Code 667, Greenbelt Road, Greenbelt, MD 20771, USA

[39]Department of Astrophysics and The Enrico Fermi Institute, University of Chicago, 5640 South Ellis Avenue, Chicago, IL 60637, USA

[40]Department of Physics and Astronomy, University of Pennsylvania, Philadephia, PA 19104, US

[41]Rutgers, the State University of New Jersey, Department of Physics and Astronomy, 136 Frelinghuysen Road, Piscataway, NJ 08854-8019, USA

[42]HH Wills Physics Laboratory, University of Bristol, Tyndall Avenue, Bristol BS8 1TL, UK

[43]Laboratoire d'Astrophysique de Marseille and Aix-Marseille Université, UMR6110 CNRS, 38 rue F. Joliot-Curie, F-13388 Marseille, France

[44]School of Mathematical Sciences, Queen Mary, University of London, Mile End Road, London, E1 4NS, UK

[45]University of Colorado, Center for Astrophysics and Space Astronomy, 389-UCB, Boulder, CO 80303, USA

[46]Department of Astronomy, University of Maryland, College Park, MD 20742 USA

[47]Observatories of the Carnegie Institution, 813 Santa Barbara Street, Pasadena, CA 91101, USA

[48]Institute for Space and Astronautical Science, Japan Aerospace Exploration Agency, 3-1-1 Yoshinodai, Chuo-ku, Sagamihara 252-5210 Japan

[49]Infrared Processing and Analysis Center, Pasadena, CA 91125, USA

[50]Jeremiah Horrocks Institute, University of Central Lancashire, Preston PR1 2HE, UK

[51]Space Science and Technology Department, Rutherford Appleton Laboratory, Chilton, Didcot, Oxfordshire OX11 0QX, UK

[52]University of British Colombia, 6224 Agricultural Road, Vancouver, BC V6T 1Z1, Canada

[53]Institute for Computational Cosmology, Durham University, Durham DH1 3LE, UK

[54]Max Planck Institut fuer Kernphysik (MPIK), Saupfercheckweg 1, 69117 Heidelberg, Germany

[55]Leiden Observatory, Leiden University, Post Office Box 9513, NL - 2300 RA Leiden, The Netherlands

* to whom correspondence should be addressed E-mail: m.negrello@open.ac.uk

Gravitational lensing is a powerful astrophysical and cosmological probe and is particularly valuable at submillimeter wavelengths for the study of the statistical and individual properties of dusty starforming galaxies. However the identification of gravitational lenses is often time-intensive, involving the sifting of large volumes of imaging or spectroscopic data to find few candidates. We used early data from the Herschel Astrophysical Terahertz Large Area Survey to demonstrate that wide-area submillimeter surveys can simply and easily detect strong gravitational lensing events, with close to 100% efficiency.

When the light from a distant galaxy is deflected by a foreground mass − commonly a massive elliptical galaxy or galaxy cluster or group − its angular size and brightness are increased, and multiple images of the same source may form. This phenomenon is commonly known as gravitational lensing (*1*) and can be exploited in the study of high-redshift galaxy structures down to scales difficult (if not impossible) to probe with the largest telescopes at present (*2–4*) and to detect intrinsically faint objects. Surveys conducted at submillimeter wavelengths can particularly benefit from gravitational lensing because submillimeter telescopes have limited spatial resolution and consequently high source confusion, which makes it difficult to directly probe the populations responsible for the bulk of background submillimeter emission (*5, 6*). In addition, galaxies detected in blank-field submillimeter surveys generally suffer severe dust obscuration and are therefore challenging to detect and study at optical and near infra-red (NIR) wavelengths. By alleviating the photon starvation, gravitational lensing facilitates follow-up observations of galaxies obscured by dust and in particular the determination of their redshift (*7*). Previous submillimeter searches for highly magnified background galaxies have predominantly targeted galaxy cluster fields (*8*). In fact, a blind search for submillimeter lensing events re-

4

quires large area because of their rarity, and sub-arcseconds angular resolutions to reveal multiple images of the same background galaxies. Although the first requirement has recently been fulfilled, thanks to the advent of the South Pole Telescope (SPT) (*9*) and the Herschel Space Observatory (Herschel) (*10*), the second is still the prerogative of ground-based interferometric facilities, such as the Submillimeter Array (SMA) and the IRAM Plateau de Bure Interferometer (PdBI), which because of their small instantaneous field of view are aimed at follow-up observations rather than large-area survey campaigns. Nevertheless, several authors (*11–14*) have suggested that a simple selection in flux density, rather than surveys for multiply-imaged sources, can be used to easily and efficiently select samples of strongly gravitationally-lensed galaxies in wide-area submillimeter and millimeter surveys. The explanation for this lies in the steepness of the number counts (the number of galaxies at a given brightness) of dust-obscured star-forming galaxies, which are usually referred to as submillimeter galaxies (SMGs) (*15*). Because of that, even a small number of highly-magnified SMGs can substantially affect the shape of the bright end of the submillimeter source counts enhancing the number of SMGs seen at bright flux densities than would be expected on the basis of our knowledge of the un-lensed SMG population (Fig.1). Furthermore, the frequency of lensing events is relatively high in the submillimeter (*11*) because SMGs are typically at high redshift ($z >\sim 1$) (*16*), and this increases the probability that a SMG is in alignment with, and therefore lensed by, a foreground galaxy. Other important contributors to the bright tail of the submillimeter counts are low-redshift ($z \leq 0.1$) spiral and starburst galaxies (*17*) and higher redshift radio-bright Active Galactic Nuclei (AGNs) (*18*); however both of these are easily identified, and therefore removed, in relatively shallow optical and radio surveys. Therefore, flux-density limited submillimeter surveys could provide a sample of lens candidates from which contaminants can be readily removed, leaving a high fraction (close to 100%) of gravitational lens systems (Fig. 1). Because this selection of lens candidates relies only on the properties of the background source

(its flux density), it can probe a wide range of lens properties (such as redshifts and masses) and thus provide a valuable sample for studying the elliptical properties of lensing galaxies ([19]) as well as investigating the detailed properties of the lensed SMGs.

The submillimeter lens candidate selection at work. Although the approach presented above may be more efficient and vastly more time-effective than those exploited so far in the radio ([20]) or the optical ([21, 22]), at least several tens of square degrees (deg^2) of the sky must be observed in the submillimeter to produce a statistically significant sample of strongly lensed objects and a minimal contamination from unlensed galaxies. This is because the surface density of lensed submillimeter galaxies is predicted to be lower than $\sim$0.5 deg^{-2}, for flux densities above 100 mJy at 500 μm (Fig. 1). Submillimeter surveys conducted before the advent of Herschel were either limited to small areas of the sky ([15, 23]), or were severely affected by source confusion due to poor spatial resolution ([24]). Therefore no previous test of this selection method has been performed, although the SPT has recently mapped an area of more than 80 deg^2 at millimetre wavelengths ([9]) and found an "excess" of sources that could be accounted for by a population of gravitationally-lensed objects.

The Herschel Astrophysical Terahertz Large Area Survey (H-ATLAS) ([25]) represents the largest-area submillimeter survey being currently undertaken by Herschel. H-ATLAS uses the Spectral and Photometric Imaging REceiver (SPIRE) ([26, 27]) and the Photodetector Array Camera and Spectrometer (PACS) ([28, 29]) instruments and, when completed, will cover $\sim$550 deg^2 of the sky from 100 to 500 μm. H-ATLAS has been designed to observe areas of the sky with previously existing multi-wavelength data: Galaxy Evolution Explorer (GALEX) ultra violet (UV) data, Sloan Digital Sky Survey (SDSS) optical imaging and spectroscopy, NIR data from the UK Infrared Telescope (UKIRT) Infrared Deep Sky Survey (UKIDSS) Large Area Survey (LAS), spectra from the Galaxy And Mass Assembly GAMA ([30]) project, radio imaging data from the

Faint Images of the Radio Sky at Twenty-cm (FIRST) survey and the NRAO Very Large Array Sky Survey (NVSS). The first $14.4\,\mathrm{deg}^2$ of the survey, centred on J2000 RA 09:05:30.0 DEC 00:30:00.0 and covering $\sim3\%$ of the total area, was observed in November 2009 as part of the Herschel Science Demonstration Phase (SDP). The results were a catalog of ~6600 sources (31) with a significance $> 5\,\sigma$, in at least one SPIRE waveband, where the noise, σ, includes both instrumental and source confusion noise and corresponds to ~7 to 9 mJy/beam.

The Herschel/SPIRE $500\,\mu$m channel is favourable for selecting lens candidates, because the submillimeter source counts steepen at longer wavelengths (24, 32). We used theoretical predictions (14) to calculate the optimal limiting flux density, above which it is straightforward to remove contaminants from the parent sample and maximize the number of strongly lensed high-redshift galaxies. The surface-density of un-lensed SMGs is predicted to reach zero by $S_{500} \sim 100\,\mathrm{mJy}$ (14) and these objects are only detectable above this threshold if gravitationally lensed by a foreground galaxy (Fig. 1). The H-ATLAS SDP catalog contains 11 sources with $500\,\mu$m flux density above 100 mJy. Ancillary data in the field revealed that six of these objects are contaminants; four are spiral galaxies with spectroscopic redshifts in the range of 0.01 to 0.05 [see (33) for a detailed analysis of one of these sources], one is an extended Galactic star forming region, and one is a previously known radio$-$bright AGN (34). Although the number of these sources are few at bright flux densities, the measured surface densities are consistent with expectations (Fig. 1) (17, 18). Exclusion of these contaminants left the five objects that form our sample of lens candidates (table S1) (35), identified as ID9, ID11, ID17, ID81 and ID130.

Unveiling the nature of the lens candidates. For gravitational lensing systems selected at submillimeter wavelengths, we would expect the lensing galaxy to be seen in optical and/or NIR images, in which the emission from the lens dominates over the higher redshift background

SMG. In line with these expectations, all of the lens candidates have a close counterpart in SDSS or UKIDSS images (or both). A likelihood ratio analysis (*36*) showed that the probability of a random association between these bright submillimeter sources and the close optical/NIR counterparts is less than a few per cent. Therefore the optical and submillimeter emissions must be physically related, either because they occur within the same object or because of the effects of gravitational lensing, boosting the flux of the background source and indirectly affecting the likelihood ratio calculations. The redshift measurements support the later scenario. Although the optical/NIR photometric/spectroscopic redshifts lie in the range of $z \sim 0.3$ to 0.9 (table 1 and figs S3 and S4) (*35*), the redshifts estimated from the submillimeter/millimeter spectral energy distributions (SED) (table 2) [following the method described in (*37, 38*)], are distinctly different (Table 1). The lensed SMG photometric redshifts have been confirmed and made more precise through the spectroscopic detection, in these objects, of carbon monoxide (CO) rotational line emission which are tracers of molecular gas assocatiated to star forming environments. Until recently, these kind of detections were difficult to achieve without prior knowledge of the source redshift, which required extensive optical/NIR/radio follow-up observations. Because of the development of wide-bandwidth radio spectrometers capable of detecting CO lines over a wide range of redshifts, it is now possible for blind redshift measurements of SMGs to be taken without relying on optical or NIR spectroscopy (*39, 40*). ID81 was observed with the Z-Spec spectrometer (*41, 42*) on the California Institute of Technology Submillimeter Observatory (CSO). The data revealed several CO lines redshifted into the frequency range of 187 to 310 GHz; the strongest of these lines has been interpreted as the CO J=7−6 line, with an estimated redshift of $z = 3.04$ (*43*). This represents the first blind redshift determination by means of Z-Spec. We followed up this observation with the PdBI and detected CO J=3−2 and CO J=5−4 emission lines, redshifted to $z = 3.042$, confirming the Z-Spec measured redshift (*35*). We also used the Zpectrometer instrument (*44, 45*) on the NRAO Robert C. Byrd

8

Green Bank Telescope (GBT) to obtain an independent confirmation of the redshift of ID81 (table 1 and fig. S1) (*35, 46*) and to measure the redshift of ID130. We detected redshifted CO J=1−0 emission at $z = 2.625$ in the spectrum of ID130 (fig. S1) (*35, 46*)]. This redshift was confirmed by the PdBI with the observation of CO J=3-2 and CO J=5-4 lines, yielding a redshift of $z = 2.626$ (*35*). The Z-Spec spectrometer observed the remaining three lens candidates (*43*) and detected CO lines at redshifts of $z = 1.577$ and $z = 1.786$ for ID9 (fig. S2) (*35*) and ID11, respectively, which are higher and inconsistent with the redshifts derived from the optical photometry/spectroscopy (Table 1). The Z-Spec CO measurements for ID17 are indicative of two redshifts; one, $z = 0.942$, that is in agreement with the optical redshift and a higher one, $z = 2.31$, which is indicative of a more distant galaxy.

To determine the morphological type of the foreground galaxies we obtained high resolution optical images for all five objects with the Keck telescope at g- and i-bands (*35*). ID9, ID11, ID81 and ID130 all have optical profiles that are consistent with elliptical galaxies (figs S5 and S6 and table S4) (*35*). The interpretation of the results for ID17 is complicated by the presence of two partially superimposed galaxies in the optical images (fig. S7) (*35*), neither exhibiting the disturbed morphology expected for lensed objects. This indicates that ID17 may be a gravitational lens system with two foreground lensing masses at similar redshifts ($z \sim 0.8$ to 0.9) − possibly a merging system − with some molecular gas responsible for the CO emission detected by Z-Spec at $z \sim 0.9$ and confirmed with optical spectroscopy (table 1). A fit to the UV/optical/NIR SEDs of ID9, ID11, ID81 and ID130 (*47*), using the models of (*48*), gives stellar masses in the range of 4×10^{10} to $15 \times M_{\odot}$ (Table 2) and almost negligible present-day star formation, which is consistent with elliptical galaxies (fig. 2).

For all five lens systems the background source appears to be undetected in the Keck g- and i-band images, despite the flux magnification due to lensing. After subtracting the best fit light profile from each lens we found no structure that could be associated with the background

source in the residual images (figs S5 and S6) (*35*). We derived 3-σ upper limits from the residual maps (table S4) (*35*) and corresponding NIR limits from the UKIDSS images. These upper limits were used to fit the SEDs of the background sources assuming the models of (*48*), calibrated to reproduce the UV-to-infrared SEDs of local, purely star-forming ultra luminous infrared galaxies (ULIRG; $10^{12} \leq L_{IR}/L_\odot < 10^{13}$) (*49*) (fig. 2). A visual extinction (*50*) of $A_V > 2$ is required to be consistent with the optical/NIR upper limits (fig. 2 and table 2), confirming severe dust obscuration in these galaxies along the line-of-sight. Our results indicate that these submillimeter bright gravitationally lensed galaxies would have been entirely missed by standard optical methods of selection.

We obtained observations at the SMA for ID81 and ID130 at $880\,\mu$m, with the aim of detecting the lensed morphology of the background galaxy (*35*). The SMA images reveal extended submillimeter emission distributed around the cores of the foreground elliptical galaxies, with multiple peaks (four main peaks in ID81 and two in ID130), which is consistent with a lensing interpretation of these structures (Fig. 3). The position of these peaks can be used to directly constrain the Einstein radius − the radius of the circular region on the sky (the Einstein ring) into which an extended source would be lensed if a foreground galaxy were exactly along the line of sight of the observer to the source (for a perfectly circular lens). The Einstein radius is a measure of the projected mass of the lens, so it can be used to derive the total (dark plus luminous) mass of the galaxy within the Einstein radius (table 2) (*35*). Another measure of the total mass of a lens is the line-of-sight stellar velocity dispersion, σ_v. We have estimated σ_v from the local Faber−Jackson (FJ) relation (*51*) between σ_v and the rest-frame B-band luminosity for elliptical galaxies. Assuming passive stellar evolution for the lens galaxies, which is appropriate for elliptical galaxies, we have extrapolated their rest-frame K-band luminosity to $z = 0$ [using the evolutionary tracks of (*52*)], and then converted this to B-band luminosity using the B - K = 4.43 color relation from (*53*). The result was then applied to the FJ relation from (*54*).

Given a mass model for the lens (*35*), we can predict the Einstein radius of the galaxy from the value of σ_v expected from the FJ relation and compare it with that directly measured from the SMA images (Table 2). Although the value of the Einstein radius derived from the line-of-sight stellar velocity dispersion is affected by large uncertainties (as a result of the scatter in the FJ relation) it is consistent with the value measured in the SMA images for both ID81 and ID130. In order to test whether the properties of the lensing galaxies in our sample are consistent with those of other known lens ellipticals at similar redshift, we compared the V-band mass-to-light ratio of the lens galaxy for ID81 and ID130 (Table 2) (*35*) to those measured in the Sloan Lens Advanced Camera for Surveys (ACS) (fig. 4) (*55*), which cover a similar redshift range (z∼0.1 to 0.3). The agreement with the average trend revealed by SLACS confirms that our lens selection method is not biased to lensing ellipticals with atypical luminosities. Moreover, the location of ID130 in Fig. 4 indicates that our selection method can probe lower masses and lower luminosity lens galaxies than those sampled by SLACS, thus offering a wider range in lens properties to be investigated.

The best fit SED to the submillimeter/millimeter photometry for each of the five background sources give infrared luminosities $L_{IR} \geq \sim 3 \times 10^{13}\,L_\odot$ (Table 2), which would classify these objects as Hyper Luminous Infra-Red galaxies (HLIRGs; $L_{IR} \geq 10^{13}\,L_\odot$). However, a correction for magnification because of lensing will reduce these values by a factor of 10 or greater. For example, assuming that the light distribution of the background source is described by a Gaussian profile with a full width at half maximum (FWHM) of 0.2 arcseconds [which is consistent with the physical extension of the background galaxy in (*4*)], the best-fit lens model (fig. S9) (*35*) predicts a total amplifications of ∼19 and ∼6 for ID81 and ID130, respectively. Typical amplifications of 8 to 10 are also suggested by (*14*), therefore, it is more likely that these sources are ULIRGs.

These results already provide constraints for models of the formation and evolution of massive

galaxies at high redshift. The fact that many (if not all) of the brightest SMGs detected in the H-ATLAS SDP field are amplified by lensing, implies that un-lensed $z > 1$ star-forming galaxies with flux densities more than $100\,\mathrm{mJy}$ at $500\,\mu\mathrm{m}$ are rare, with ≤ 4.6 of them per $14.4\,\mathrm{deg}^{-2}$, at 99% probability (assuming Poisson statistics). This translates into a $0.32\,\mathrm{deg}^{-2}$ upper limit on the surface density of these sources. The same limit should translate to the abundance of HLIRGs with $\mathrm{L_{IR}} > 5\times10^{13}\,\mathrm{L_\odot}$ at $z < 4$, because they would also have 500-$\mu\mathrm{m}$ flux densities above $100\,\mathrm{mJy}$, which has possible implications for the role of feedback during the formation of the most massive galaxies in the universe. By extrapolating our SDP findings to the full H-ATLAS field, we predict a total sample of more than 100 bright lensed sources, with which we can further improve this constraint.

References and Notes

1. When multiple images of the same background source are formed, the event is known as strong gravitational lensing .

2. P. J. Marshall, *et al.*, *Astrophys. J.* **671**, 1196 (2007).

3. D. P. Stark, *et al.*, *Nature* **455**, 775 (2008).

4. A. M. Swinbank, *et al.*, *Nature* **464**, 733 (2010).

5. I. Smail, R. J. Ivison, A. W. Blain, *Astrophys. J. L.* **490**, L5+ (1997).

6. A. W. Blain, J. Kneib, R. J. Ivison, I. Smail, *Astrophys. J. L.* **512**, L87 (1999).

7. M. Rowan-Robinson, *et al.*, *Nature* **351**, 719 (1991).

8. I. Smail, R. J. Ivison, A. W. Blain, J. Kneib, *Mon. Not. R. Astron. Soc.* **331**, 495 (2002).

9. J. D. Vieira, *et al.*, *Astrophys. J.* **719**, 763 (2010).

10. G. L. Pilbratt, *et al.*, *Astron. & Astrophys.* **518**, L1+ (2010).

11. A. W. Blain, *Mon. Not. R. Astron. Soc.* **283**, 1340 (1996).

12. F. Perrotta, C. Baccigalupi, M. Bartelmann, G. De Zotti, G. L. Granato, *Mon. Not. R. Astron. Soc.* **329**, 445 (2002).

13. F. Perrotta, *et al.*, *Mon. Not. R. Astron. Soc.* **338**, 623 (2003).

14. M. Negrello, *et al.*, *Mon. Not. R. Astron. Soc.* **377**, 1557 (2007).

15. K. Coppin, *et al.*, *Mon. Not. R. Astron. Soc.* **372**, 1621 (2006).

16. S. C. Chapman, A. W. Blain, I. Smail, R. J. Ivison, *Astrophys. J.* **622**, 772 (2005).

17. S. Serjeant, D. Harrison, *Mon. Not. R. Astron. Soc.* **356**, 192 (2005).

18. G. de Zotti, *et al.*, *Astron. & Astrophys.* **431**, 893 (2005).

19. L. V. E. Koopmans, T. Treu, A. S. Bolton, S. Burles, L. A. Moustakas, *Astrophys. J.* **649**, 599 (2006).

20. I. W. A. Browne, The Class Collaboration, *Gravitational Lensing: Recent Progress and Future Go*, T. G. Brainerd & C. S. Kochanek, ed. (2001), vol. 237 of *Astronomical Society of the Pacific Conference Series*, pp. 15–+.

21. M. Oguri, *et al.*, *Astron. J.* **132**, 999 (2006).

22. C. Faure, *et al.*, *Astrophys. J. S.* **176**, 19 (2008).

23. A. Weiß, *et al.*, *Astrophys. J.* **707**, 1201 (2009).

24. M. J. Devlin, *et al.*, *Nature* **458**, 737 (2009).

25. S. Eales, *et al.*, *Publ. Astron. Soc. Pac.* **122**, 499 (2010).

26. M. J. Griffin, *et al.*, *Astron. & Astrophys.* **518**, L3+ (2010).

27. E. Pascale, *submitted; preprint available at http://xxx.lanl.gov/abs/astro-ph/1010.5782* .

28. A. Poglitsch, *et al.*, *Astron. & Astrophys.* **518**, L2+ (2010).

29. E. Ibar, *submitted; preprint available at http://xxx.lanl.gov/abs/astro-ph/1009.0262* .

30. S. Driver, *submitted; preprint available at http://xxx.lanl.gov/abs/astro-ph/1009.0614* .

31. E. E. Rigby, *submitted; preprint available at http://xxx.lanl.gov/abs/astro-ph/1010.5787* .

32. D. L. Clements, *et al.*, *Astron. & Astrophys.* **518**, L8+ (2010).

33. M. Baes, *et al.*, *Astron. & Astrophys.* **518**, L39+ (2010).

34. J. González-Nuevo, *et al.*, *Astron. & Astrophys.* **518**, L38+ (2010).

35. Supporting online material (SOM) .

36. D. J. B. Smith, *et al.*, *submitted; preprint available at http://xxx.lanl.gov/abs/astro-ph/1007.5260* .

37. D. H. Hughes, *et al.*, *Mon. Not. R. Astron. Soc.* **335**, 871 (2002).

38. I. Aretxaga, *et al.*, *Mon. Not. R. Astron. Soc.* **342**, 759 (2003).

39. A. Weiß, *et al.*, *Astrophys. J. L.* **705**, L45 (2009).

40. E. Daddi, *et al.*, *Astrophys. J. L.* **695**, L176 (2009).

41. B. J. Naylor, *et al.*, *Society of Photo-Optical Instrumentation Engineers (SPIE) Conference Series*, T. G. Phillips & J. Zmuidzinas, ed. (2003), vol. 4855 of *Presented at the Society of Photo-Optical Instrumentation Engineers (SPIE) Conference*, pp. 239–248.

42. C. M. Bradford, *et al.*, *Astrophys. J.* **705**, 112 (2009).

43. R. Lupu, *submitted; preprint available at http://xxx.lanl.gov/abs/astro-ph/1009.5983* .

44. A. I. Harris, *et al.*, *From Z-Machines to ALMA: (Sub)Millimeter Spectroscopy of Galaxies*, A. J. Baker, J. Glenn, A. I. Harris, J. G. Mangum, & M. S. Yun , ed. (2007), vol. 375 of *Astronomical Society of the Pacific Conference Series*, pp. 82–+.

45. The Zpectrometer frequency coverage allows it to search for CO J=1−0 transition over the redshift range 2.2 to 3.5 simultaneously .

46. D. Frayer, *submitted; preprint available at http://xxx.lanl.gov/abs/astro-ph/1009.2194* .

47. Only g and i-band photometry can be obtained for each of the two galaxies detected in ID17. For this reason, we did not attempt any fit to the optical/NIR SED of this H-ATLAS source .

48. E. da Cunha, S. Charlot, D. Elbaz, *Mon. Not. R. Astron. Soc.* **388**, 1595 (2008).

49. E. da Cunha, *et al.*, *in press; preprint available at http://xxx.lanl.gov/abs/astro-ph/1008.2000* .

50. The visual extinction parameter, A_V, is the difference between the observed V-band magnitude and the intrinsic (dust-free) V-band magnitude of the galaxy .

51. S. M. Faber, R. E. Jackson, *Astrophys. J.* **204**, 668 (1976).

52. C. J. Willott, S. Rawlings, M. J. Jarvis, K. M. Blundell, *Mon. Not. R. Astron. Soc.* **339**, 173 (2003).

53. J. Huang, L. L. Cowie, G. A. Luppino, *Astrophys. J.* **496**, 31 (1998).

54. D. H. Gudehus, *Astrophys. J.* **382**, 1 (1991).

55. M. W. Auger, *et al.*, *Astrophys. J.* **705**, 1099 (2009).

Tables

Table 1: Photometric and spectroscopic redshifts of the five lens candidates. Spectroscopic redshifts were derived from optical lines for the lens [$z_{\mathrm{spec}}^{(\mathrm{opt})}$] and from CO lines for the background source [$z_{\mathrm{spec}}^{(\mathrm{CO})}$]. Photometric redshifts are based on UV/optical/NIR photometry for the lens [$z_{\mathrm{ot}}^{(\mathrm{opt})}$] and H-ATLAS plus SMA and Max-Planck Millimeter Bolometer (MAMBO) photometry for the background source[$z_{\mathrm{phot}}^{(\mathrm{submillimeter/millimeter})}$; using the photometric redshift code of (*37, 38*)]. The quoted errors on the redshifts correspond to a 68% confidence interval.

SDP ID	$z_{\mathrm{phot}}^{(\mathrm{opt})}$	$z_{\mathrm{spec}}^{(\mathrm{opt})}$	$z_{\mathrm{phot}}^{(\mathrm{sub-mm/millimeter})}$	$z_{\mathrm{spec}}^{(\mathrm{CO})}$
9	0.679±0.057	–	$1.4^{+0.3}_{-0.4}$	1.577±0.008[1]
11	0.72±0.16	0.7932±0.0012[2]	$1.9^{+0.4}_{-0.3}$	1.786±0.005[1]
17	0.77±0.13	0.9435±0.0009[2]	$2.0^{+0.4}_{-0.3}$	0.942±0.004 & 2.308±0.011[1]
81	0.334±0.016	0.2999±0.0002[3]	$2.9^{+0.2}_{-0.3}$	3.037±0.010[1]
				3.042±0.001[4],[5]
130	0.239±0.021	0.2201±0.002[6]	$2.6^{+0.4}_{-0.2}$	2.625±0.001[4]
				2.6260±0.0003[5]

[1] Datum is from CSO/Z-Spec (*43*)

[2] Datum is from the William Herschel Telescope (*35*)

[3] Datum is from SDSS

[4] Datum is from GBT/Zpectrometer (*46*)

[5] Datum is from PdBI (*35*)

[6] Datum is from the Apache Point Observatory (*35*)

Table 2: Derived parameters for the five lens candidates. Estimated mass in stars (M$_\star$) and Star Formation Rate (SFR) of the foreground galaxy derived from the best-fit to the UV/optical/near-IR part of the SED; the Einstein radius measured from the SMA images ($\theta_{\rm E}$); mass within the Einstein radius (M$_{\rm E}$) estimated from $\theta_{\rm E}$; line-of-sight stellar velocity dispersion ($\sigma_{\rm v}^{\rm FJ}$) derived from the Faber-Jackson relation and the B-band luminosity produced by the best-fit to the UV/optical/NIR SED; Einstein radius ($\theta_{\rm E}^{\rm FJ}$) calculated from $\sigma_{\rm v}^{\rm FJ}$; infrared luminosity of the background source (L$_{\rm IR}$), without correction for magnification, derived by fitting the submillimeter/millimeter part of the SED and the upper limits at optical and NIR wavelengths (Fig. 2); and visual extinction parameter (A$_V$) inferred for the background galaxy. All the quoted errors correspond to a 68 per cent confidence interval. For ID17 only the infrared luminosity and the extinction parameter of the background source are quoted because the lensing mass probably consists of two galaxies that can only be disentangled in the Keck images. The symbols M$_\odot$ and $L_\odot$ denote the total mass and the total luminosity of the Sun, respectively, and correspond to $M_\odot = 1.99 \times 10^{30}$ kg and $L_\odot = 3.839 \times 10^{33}$ erg s^{-1}. Dashes indicate lack of constraints.

| H-ATLAS ID	log(M$_\star$) (M$_\odot$)	log(SFR) (M$_\odot$ yr^{-1})	$\theta_{\rm E}$ (arcsec)	log(M$_{\rm E}$) (M$_\odot$)	$\sigma_{\rm v}^{\rm FJ}$ (km sec^{-1})	$\theta_{\rm E}^{\rm FJ}$ (arcsec)	log(L$_{\rm IR}$) (L$_\odot$ ^{a})	A$_V$
9	$10.79^{+0.16}_{-0.11}$	$-0.51^{+0.20}_{-0.27}$	—	—	232^{+75}_{-56}	$0.77^{+0.49}_{-0.34}$	$13.48^{+0.07}_{-0.06}$	$6.7^{+1.5}_{-1.0}$
11	$11.15^{+0.09}_{-0.10}$	$-0.08^{+0.18}_{-0.24}$	—	—	258^{+82}_{-62}	$0.91^{+0.59}_{-0.40}$	$13.61^{+0.06}_{-0.06}$	$5.1^{+1.6}_{-0.7}$
17	—	—	—	—	—	—	$13.57^{+0.08}_{-0.06}$	$5.3^{+1.4}_{-0.6}$
81	$11.17^{+0.04}_{-0.08}$	$-1.66^{+0.46}_{-0.14}$	1.62 ± 0.02	11.56 ± 0.01	242^{+77}_{-58}	$1.51^{+0.98}_{-0.67}$	$13.71^{+0.07}_{-0.07}$	$3.5^{+3.4}_{-0.3}$
130	$10.65^{+0.06}_{-0.08}$	$-1.17^{+0.39}_{-0.58}$	0.59 ± 0.02	10.57 ± 0.04	174^{+55}_{-42}	$0.81^{+0.52}_{-0.36}$	$13.45^{+0.08}_{-0.09}$	$1.9^{+0.3}_{-0.3}$

Figures
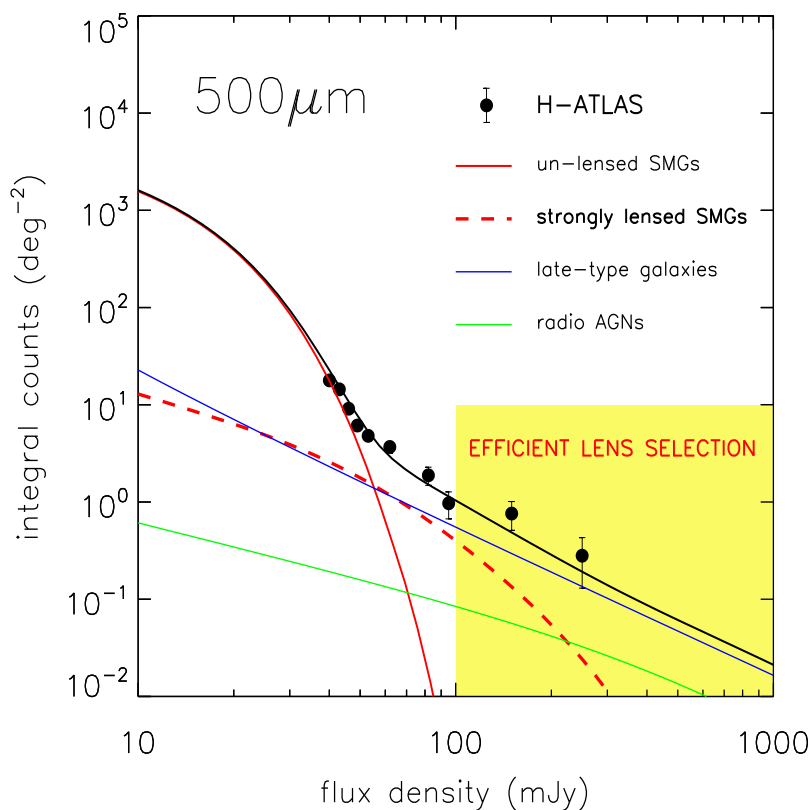
Figure 1: Selection of gravitational lenses at submillimeter wavelengths. The 500 μm source counts consist of three different populations (*14*): high-redshift SMGs; lower redshift late type (starburst plus normal spiral) galaxies; and radio sources powered by active galactic nuclei. Strongly lensed SMGs dominate over unlensed SMGs at very bright fluxes where the count of un-lensed SMGs falls off dramatically (yellow shaded region). The data points are from H-ATLAS (*32*).
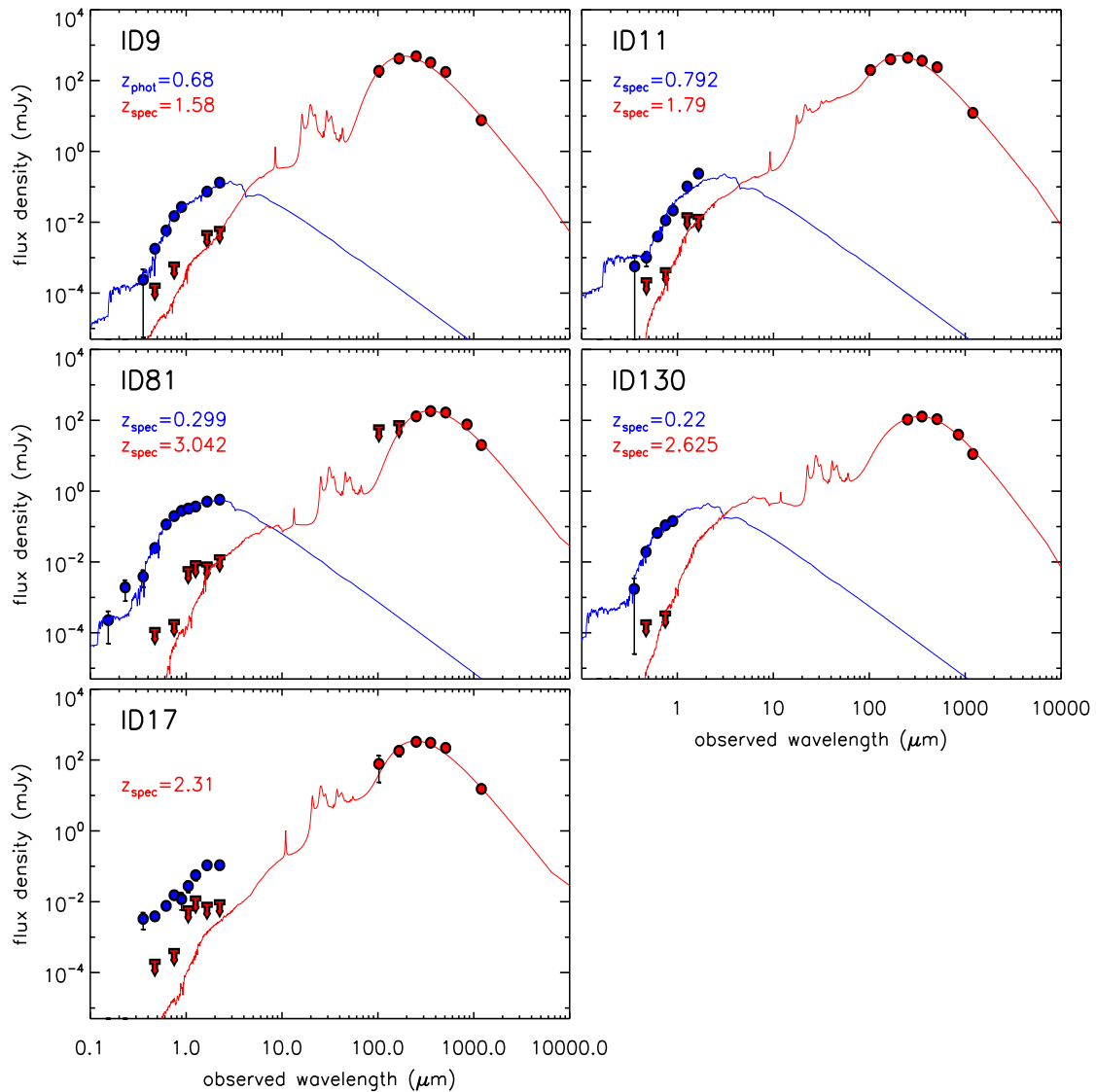
Figure 2: Spectra of the gravitational lens candidates. The UV, optical and NIR data points (blue dots) are from *GALEX*, SDSS and UKIDSS LAS, respectively. The submillimeter/millimeter data points (red dots) are from PACS/Herschel, SPIRE/Herschel, SMA and Max-Planck Millimeter Bolometer (MAMBO)/IRAM. Upper limits at PACS/Herschel wavelengths are shown at $3\,\sigma$. ID130 lies outside the region covered by PACS. The photometric data were fitted using SED models from (*48*). The background source, responsible for the submillimeter emission, is a heavily dust obscured star-forming galaxy (red solid curve), whereas the lens galaxy, which is responsible for the UV/optical and NIR part of the spectrum, is caracterized by passive stellar evolution.
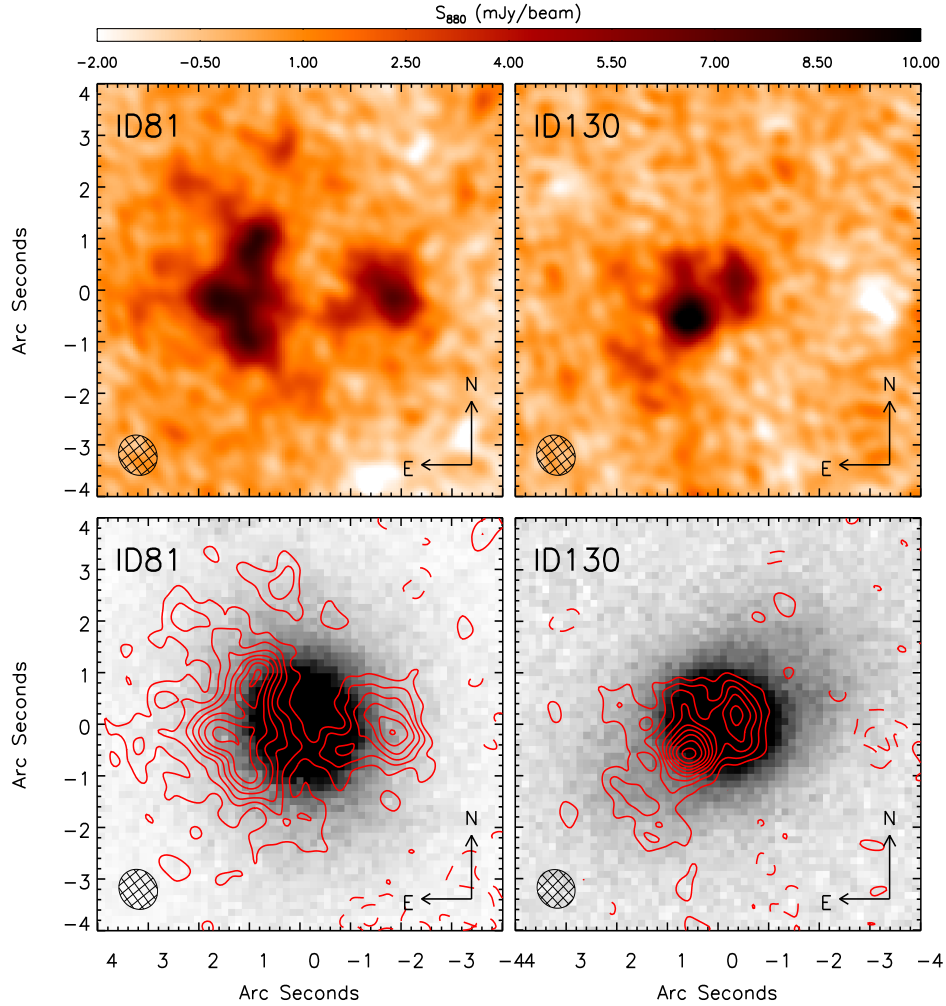
Figure 3: Submillimeter and optical follow-up imaging of ID81 and ID130. The SMA images of ID81 and ID130 are shown in the top panels, centered on the optical counterpart, and were obtained by combining the visibility data from very-extended, compact and sub-compact configuration observations. The Keck i-band image of ID81 and ID130 are shown in the bottom panels with the SMA contours superimposed (in red). The contours are in steps of -2σ, 2σ, 4σ, 6σ, 8σ, 10σ... , with $\sigma = 0.6\,\mathrm{mJy/beam}$. The SMA synthesized beam is shown in the bottom-left corner.
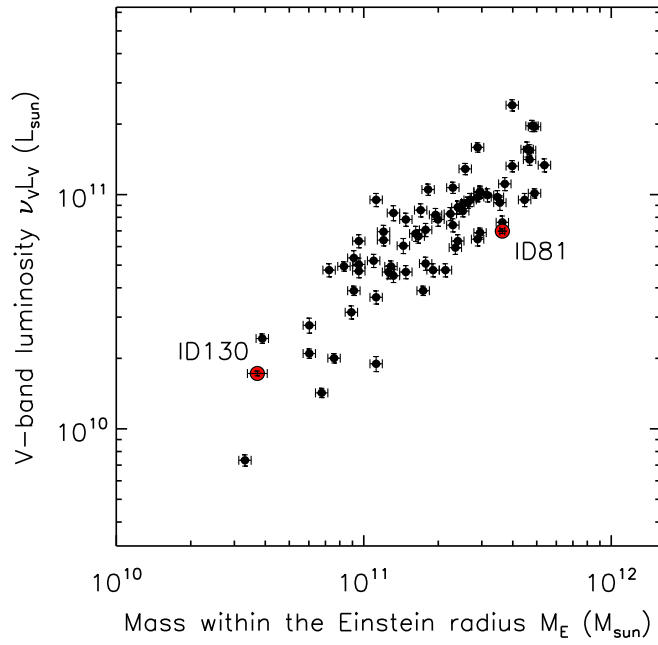
Figure 4: Relationship between mass and luminosity for the lensing galaxy in ID81 and ID130. The rest-frame $V-$band luminosity was derived from the best-fit SED to the UV/optical/NIR photometric data; the mass within the Einstein radius is that measured directly from the SMA images. The light versus mass relation inferred for ID81 and ID130 (red dots) is consistent with that observed for the SLACS lenses [black dots, from (55) assuming an uncertainty of 0.025dex in their mass estimates].

Supporting Online Material

MAMBO observations

The five H-ATLAS/SDP lens candidates, i.e. ID9, ID11, ID17, ID81 and ID130, were observed on 2010 March 9 and 10, with MAMBO, at the IRAM 30 meter telescope on Pico Veleta, in Diretcor's Discretionary Time (DDT). The MAMBO array consists of 117 bolometer elements and operates at a central frequency of $250\,\mathrm{GHz}$, corresponding to $1.2\,\mathrm{mm}$. The beam size (FWHM ≈ 11 arcsec) of MAMBO ensures that the true dust emission at $1.2\,\mathrm{mm}$ is obtained if the source is not more extended than a few arcseconds. Each science target was observed in the photometric mode ("on-off") of MAMBO which is based on the chop-nod technique and placing the target on a reference bolometer element (on-target channel). The total observing time was 1.5 hours. Data were reduced using MOPSIC, and the current version of MOPSI (Zylka 1998, The MOPSI Cookbook (Bonn: MPIfR)).

Keck observations

The imaging observations were acquired on 10 March 2010 using the dual-arm Low Resolution Imaging Spectrometer [LRIS; (*1, 2*)] on the 10-m Keck I telescope. Each target field received simultaneous $110 \times 3\,\mathrm{s}$ integrations with the g-filter and $60 \times 3\mathrm{s}$ integrations with the i-filter using the blue and red arms of LRIS. A $\sim 20''$ dither pattern was employed to generate on-sky flat field frames when incorporating all five fields. In addition, $1\,\mathrm{s}$ integrations were acquired in

the g- and i-filters for photometric calibration of bright stars in each field. The seeing FWHM for the science exposures was $\sim 0.8 - 0.9''$. The data were reduced using IDL routines and combined and analysed using standard IRAF tasks.

SMA observations

Observations of two H-ATLAS/SDP sources, ID81 and ID130, were obtained at $880\,\mu$m using the only current high resolution submillimeter facility in the world, the SMA. The SMA is an interferometer located near the summit of Mauna Kea, Hawaiim and consists of eight 6 m diameter radio telescopes. The two H-ATLAS sources were observed in Director's Discretionary Time (from February to May 2010) in three separate configurations, with baselines spanning a spatial range from 6 to 509 meters, over a total of 4 observing periods (Table S3).

Target observations from each period were interspersed with observations of calibration sources, quasars J0909+013 and J0825+031 (phase) and J0730-116 and J0854+201 (amplitude). The phase calibration targets were typically observed every 7 to 15 minutes, depending upon configuration (a faster cycle was used for the larger configurations).

Calibration of the complex visibility data was performed within the SMA's MIR package, a suite of IDL-based routines designed for use with SMA data. The initial opacity correction was obtained through application of system temperature to the raw visibility data, a standard practice. Further complex gain corrections, to remove both atmospheric and instrumental amplitude and phase variations, were measured using the calibration quasars, which appear as point sources to the interferometer. Calibration of the absolute flux density scale was performed using measurements of Titan, whose continuum and line structure is known to within about 5% at submillimeter/millimeter wavelengths.

The resulting calibrated visibility data for each source were combined and imaged within the NRAO Astronomical Image Processing System (AIPS). Photometry obtained for the SMA images along with those from PACS, SPIRE, MAMBO are given in table S1.

Plateau de Bure Interferometer observations

The H-ATLAS/SDP sources ID81 and ID130 were observed in the CO J=3-2 and CO J=5-4 lines with the IRAM Plateau de Bure Interferometer (*3*). Both sources were observed in excellent atmospheric conditions and with the full sensitivity of the six-element array. The observing frequencies were based on the redshifts provided by the CSO/Z-spec spectrometer. The receiver bandwidth was adjusted for maximum sensitivity and the observing frequencies centered in the 1 GHz baseband of the narrowband correlator. Observations of ID81 were made on March 22, 2010 for an effective integration time of 22 min and 14 min, respectively, for the CO J=3-2 and J=5-4 lines. The RF calibration was measured on 3C84, and amplitude and phase calibrations were made on 0823+033. The J=3-2 and J=5-4 transitions in ID130 were observed on March 26 and April 16, 2010, respectively, for an effective integration time of 74 min and 32 min. The RF calibration was measured on 3C273, and amplitude and phase calibrations were made on 0906+015. The absolute flux calibration scales for ID81 and ID130 were established using as primary calibrator MWC349. Data reduction and calibration were made using the GILDAS software package in the standard antenna based mode.

Optical spectroscopic observations

Optical spectroscopic observations of ID11 and ID17 were made using the ISIS double-arm spectrograph on the 4.2-m William Herschel Telescope (WHT). The R158B and R158R gratings were used to provide wavelength coverage across the entire optical spectrum, split by a dichroic at $\sim$5300 Å. Four 900-second exposures were taken of each source in a standard 'ABBA' pattern, nodding the telescope along the slit by 10 arcseconds between the first and second exposures, and back to the original position between the third and fourth integrations. This allowed initial sky subtraction to be performed by simply subtracting the 'A' frames from the 'B' frames. Additional sky subtraction was performed by subtracting the median value of each row, and then the positive and negative beams were aligned and coadded. Wavelength calibration was performed using observations of arc lamps taken with the same set-up. A one-dimensional spectrum was then optimally extracted. The spectra were taken through thin cloud and therefore no attempt has been made to flux-calibrate them. There was very little signal in the blue arms and so only the red-arm spectra are presented here. The redshifts of the two sources were determined by cross-correlation with template spectra. All reduction steps were undertaken using the IRAF package. The resulting spectra are shown in Fig. S3. The spectrum of ID11 reveals absorption lines associated to singly ionised calcium Ca H+K (rest-frame wavelengths: 3968.5 Å for H-line and 3933.7 Å for K-line) and the 4000 Å break feature (rest-frame wavelength 4000 Å) at $z = 0.793$, while the spectrum of ID17 shows the emission from oxygen doublet [OII]3727 (rest-frame wavelengths 3726-3729 Å) and the 4000 Å break feature at $z = 0.944$. In both spectra the absorption feature observed at ~ 7600 Å is due to the Earth's atmosphere.

A 30-minute exposure of ID130 was taken on May 15, 2010, with the Apache Point Observatory's 3.5-meter telescope and the DIS [Dual Imaging Spectrograph, (*4*)] long-slit spectrograph through medium clouds at an average airmass of 1.5. The spectrum was processed by subtracting the detector bias, dividing by a flat-field frame to correct for variable pixel response,

performing distortion correction to align the spectrum in the wavelength and spatial directions, subtracting the sky flux determined from parts of the slit containing no sources, and applying a wavelength calibration by reference to emission lines from a Helium-Neon-Argon calibration lamp. Two emission lines in the spectrum (Fig. S4) were identified as [O II]3727 and [Ne III]3869 (rest-frame wavelengths 3869 $\mathring{A}$) from the ratio of their observed wavelengths. From the ratio of their observed to emitted wavelengths the redshift of the galaxy was determined to be $z =$0.2201±0.002.

Modelling with GALFIT

GALFIT (*5*) is a publicly available two-dimensional non-linear fitting algorithm, which allows galaxy images to be modelled with one or multiple analytical light profiles. Each profile is constrained by a function and a set of parameters. GALFIT convolves the profiles with a user supplied point spread function, in this case empirical point spread functions constructed using nearby stars, and then performs a least-squares minimisation. No hard or soft constraints were applied to the fitting parameters to avoid any prior on the galaxy morphological type. For ID9 and ID11 single Sersic profiles resulted in a reduced χ^2 close to 1.0 (see table S4 for the best fit parameters). ID17 was fitted with two Sersic component, assuming two lensing galaxies. The resulting Sersic indices were both less than 1 (see table S4). For ID81 and ID130 two components were necessary to achieve a satisfactory fit, with a clean residual. The best fits were obtained using a combination of a compact elliptical Sersic core plus an exponential disk. No detectable background structure was revealed after subtracting the models, which shows the background galaxy is below the optical detection limit. Postage stamp images of ID9, ID11, ID17, ID81 and ID130 are shown in Figs S5 and S6, together with the corresponding best-fit models and residuals, while Fig. S7 shows the individual GALFIT components for ID81 and ID130.

To derive photometric upper limits, we performed random aperture photometry on the i- and g-band Keck maps, using a 1.5 arcsecond radius. This radius was chosen to correspond with the structure visible in the SMA images for ID81 and ID130, which extends to regions with radii of approximately $1-1.5$ arcseconds. The resulting flux distributions were fitted with Gaussians and the $3-\sigma$ upper limits are presented in Table S4.

Mass estimate from lensing

The Einstein radius of a strong galaxy-galaxy gravitational lens system can be measured from the configuration of multiple lensed images by averaging the distances of the images from the center of the lensing galaxy. For two of the H-ATLAS/SDP lens candidates, ID81 and ID130, the positions of the lensed images are constrained by high-resolution SMA follow-up imaging. The lensed images of the background sources appear as peaks in the SMA signal-to-noise ratio map. Here we have selected those peaks with signal-to-noise ratio above eight, which provided positions for four images in ID81 and two images in ID130. The error on the Einstein radius is estimated by taking into account the uncertainties on the position of the individual peaks. For a point source the rms error on its position is $\sqrt{2}\sigma/$SNR (assuming no systematic astrometry errors and uncorrelated Gaussian noise), where σ is the Gaussian rms width of the instrument beam ($=$FWHM/$2\sqrt{2\ln2}$), while SNR is the signal-to-noise ratio at the source position (6, 7). The SMA synthesised beam (derived by combining observations in VEX, COM and SUB configurations) has size $0.81''\times0.73''$ for ID81 and $0.78''\times0.72''$ for ID130. Therefore, in estimating the relative positional uncertainty of the peaks, we have assumed FWHM=$0.75''$ and FWHM=$0.77''$ for ID81 and ID130, respectively. The absolute positional uncertainty of the SMA images is estimated by referencing the data to nearby point-like sources (quasars) of known positions and is below 10 milli-arcseconds.

Once the Einstein radius is known, the mass within the Einstein ring can be easily derived assuming a Singular Isothermal Sphere (SIS) model (although the result is only little dependent on the model used) which is characterized by a projected surface density that falls off as θ^{-1}, where θ is the angular distance from the center of the mass distribution (8),

$$M_{\mathrm{E}} = M(< \theta_{\mathrm{E}}) = \pi\Sigma_{\mathrm{crit}}\theta_{\mathrm{E}}^2, \tag{1}$$

and Σ_{crit} is the *critical surface density*:

$$\Sigma_{\text{crit}} = \frac{c^2}{4\pi G} \frac{D_{\text{S}}}{D_{\text{L}} D_{\text{LS}}}. \tag{2}$$

In the equation above, c is the speed of light, G is the gravitational constant, D_{L} and D_{S} are the angular diameter distances to the lens and the source, respectively, while D_{LS} is the angular diameter distance between the lens and the source. The error on the mass is obtained by propagating the errors on the Einstein radius and on the spectroscopic/photometric redshifts used to derived the angular diameter distances. The estimated values of θ_{E} and M_{E} are listed in Table 2.

Gravitational lensing modeling

A detailed analysis of the lensed structure revealed by the SMA images is beyond the scope of this paper and is deferred to a forthcoming publication. However, in order to prove that such a structure is consistent with a lensing event, we have used the publicly available LENSMODEL software (*9*) to reproduce the positions of the peaks in the SMA maps. We have assumed a Singular Isothermal Ellipsoid (SIE) model (*8*) for the mass distribution of the lens galaxy. The SIE model consists of concentric and aligned elliptical isodensity contours with axis ratio q. The circular limit is the SIS model and corresponds to $q = 1$. The results are shown in Fig. S9. We have further assumed that the centroid of the mass model coincides with that of the light distribution of the lensing galaxy. The best-fit model for ID130 has ellipticity $e = 0.16$ and position angle (measured East of North) of $\theta = +75\,$deg, consistent with the results found for the optical light-distribution that is dominated by the more compact Sersic profile (Table S4 and Fig. S8). For ID81, the mass distribution has ellipticity $e = 0.24$ and position angle $\theta = -3\,$deg, which is not consistent with that measured for the luminous component (Table S4 and Fig. S8). Besides, the position of the peaks is not well reproduced by the model. This may hint at the effect of an external shear (which we did not include) due to a nearby cluster (photometrically detected 3.6 arcminutes away), in the direction indicated by the arrow in Fig. S9.

We have used the best-fit lens models to approximatively quantify the magnification experienced by a background source described by a Gaussian profile with a Full Width at Half Maximum (FWHM) in the range 0.1-0.3″. This extension is consistent with the physical size of the submillimeter galaxy studied by (*10*). The inferred magnification is ∼18-31 for ID81 and ∼5-7 for ID130. An example of lensed image, after convolution with the SMA point spread function, for the case FWHM=0.2″ is shown in Fig. S9.

Figures

Figure S 1: CO line detections in ID81 and ID130. The figure shows the difference between the spectrum of ID81 and that of ID130, derived from Zpectrometer observations. The relative spectrum is normalized such that the peak line strength of ID81 is equal to 1. In both objects the peak is associated with the CO J=1-0 emission line (rest-frame frequency 115.27 GHz).
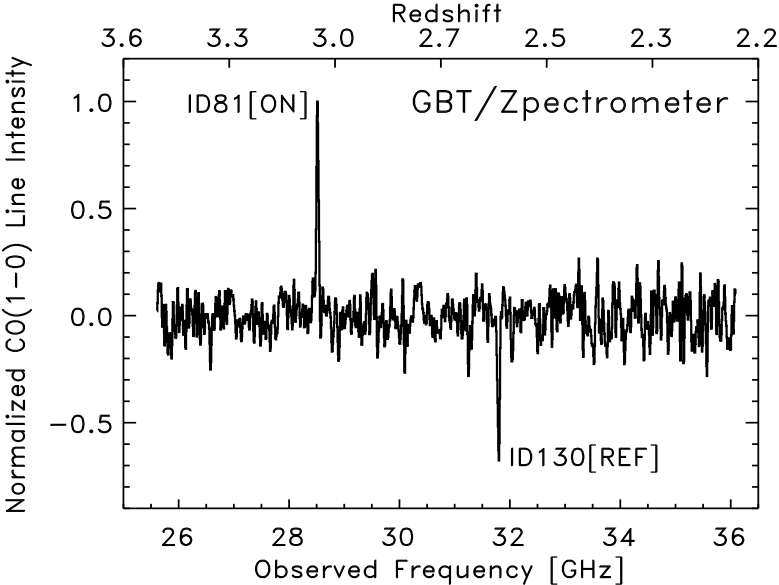
Figure S 2: CO line detections in ID9. The figure shows the spectrum derived from Z-Spec observations. The CO emission lines redshifted into the frequency range probed by Z-Spec correspond to transitions J=5-4 (rest-frame frequency 576.3 GHz) and J=6-5 (rest-frame frequency 691.5 GHz).
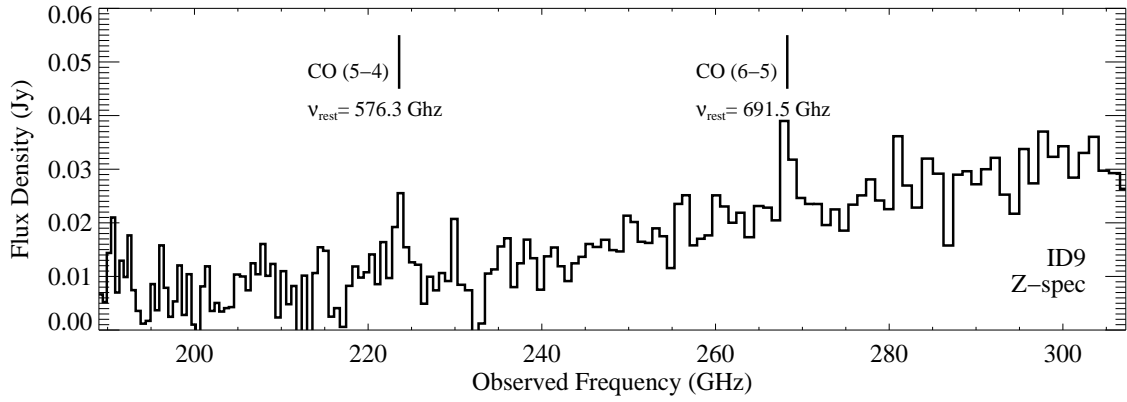

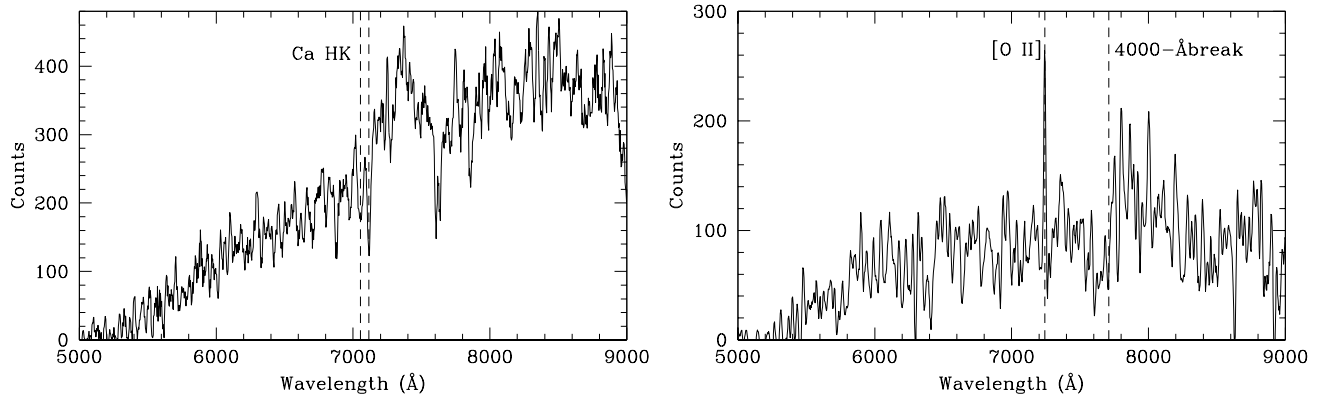Figure S 3: Optical spectra of ID11 and ID17 obatined with the WHT.

Figure S 4: Optical spectrum of ID130 obtained with the APO telescope. The bottom panel of the figure shows the reduced 2-d spectrum in the region of the detected emission lines. The top panel shows the flux summed in a 5-pixel wide (2 arcsecond) aperture centered on the object, with an arbitrary flux scale because the clouds made wavelength calibration impossible.
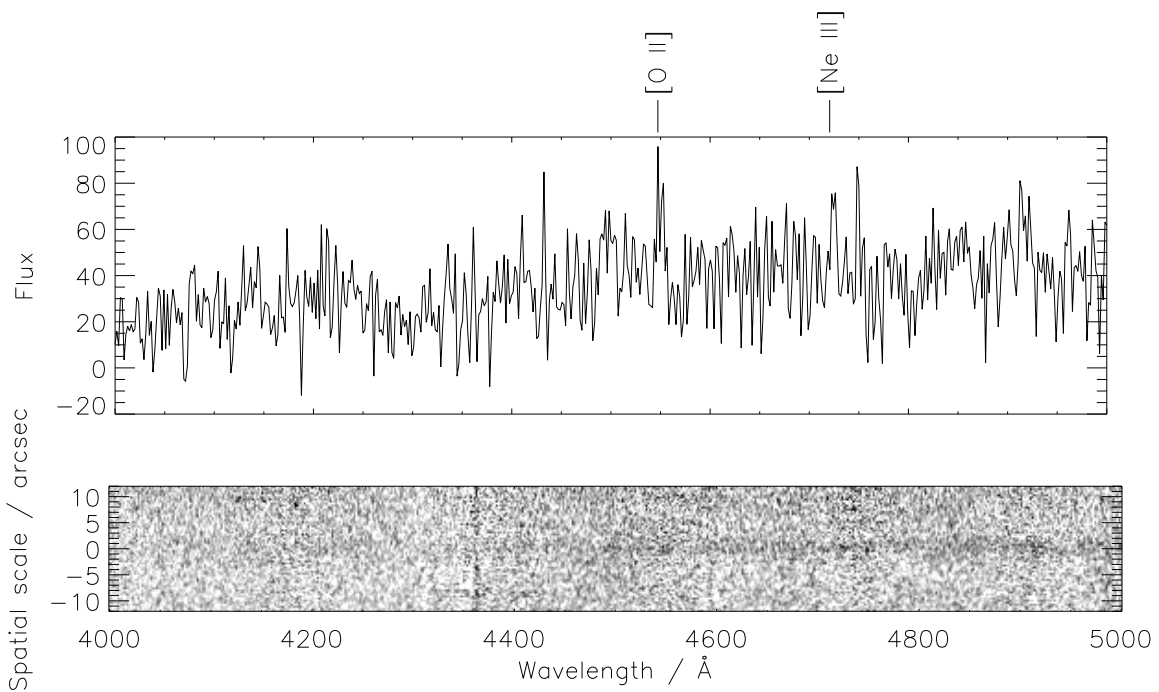
Figure S 5: Best-fit to the light distribution of the lens galaxy in the gravitational lens systems ID9, ID11 and ID17. The postage stamp images show, from left to right, the keck i-band image, the best-fit light distribution model provided by GALFIT and the residual map obtained by subtracting the best-fit model from the observed light distribution. The map of the residuals show no evident structure, implying that the background source is particularly faint in the optical, despite the magnification due to lensing.
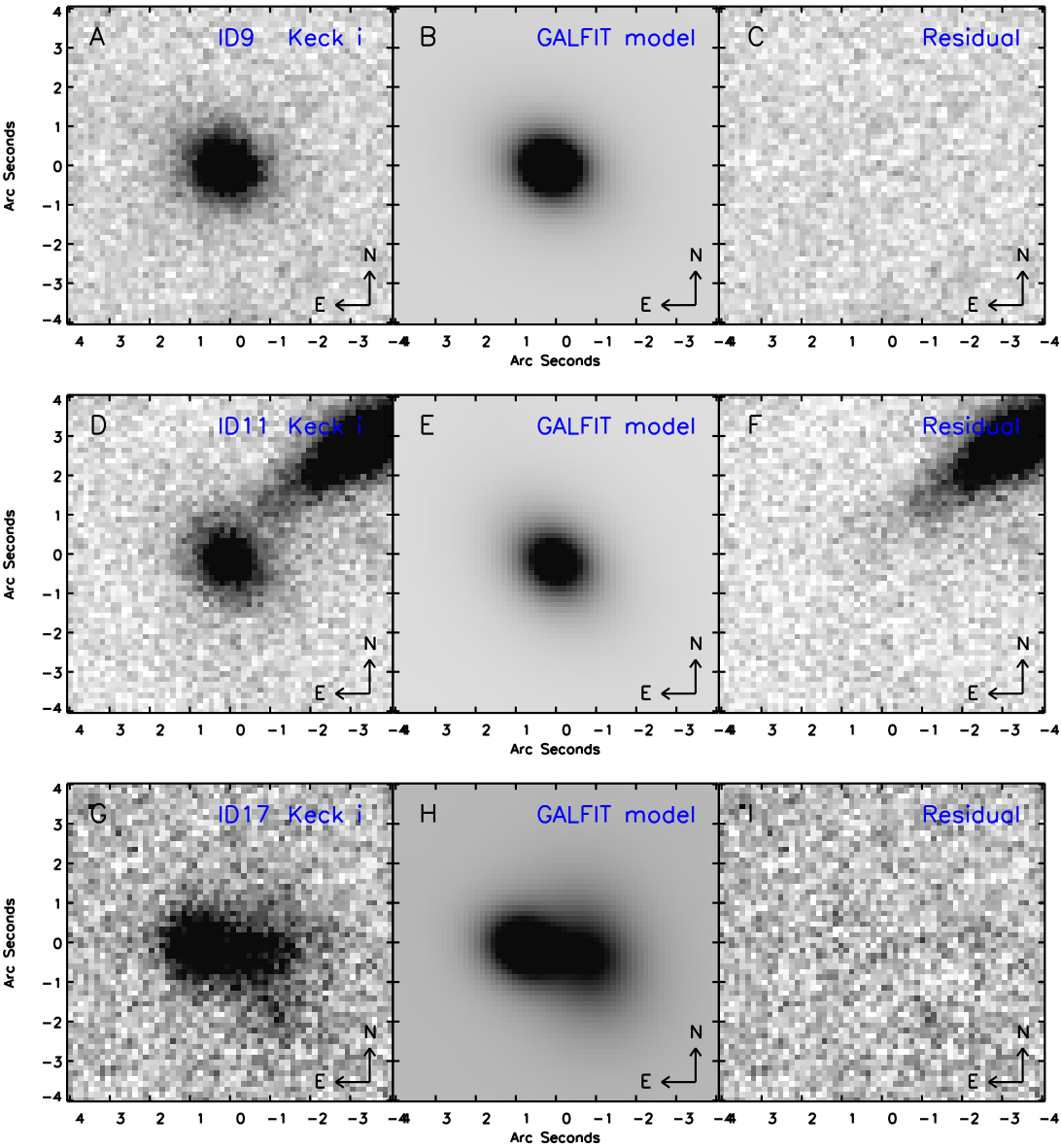
Figure S 6: Best-fit to the light distribution of the lens galaxy in the gravitational lens systems ID81 and ID130. The postage stamp images show, from left to right, the keck i-band image, the best-fit light distribution model provided by GALFIT and the residual map obtained by subtracting the best-fit model from the observed light distribution. The SMA contours (in red) are overlaid on the optical images (in steps of 6σ, 8σ, 10σ, etc.) to highlight that there is no evident correspondence between the submillimeter and the optical emission in the residual maps.
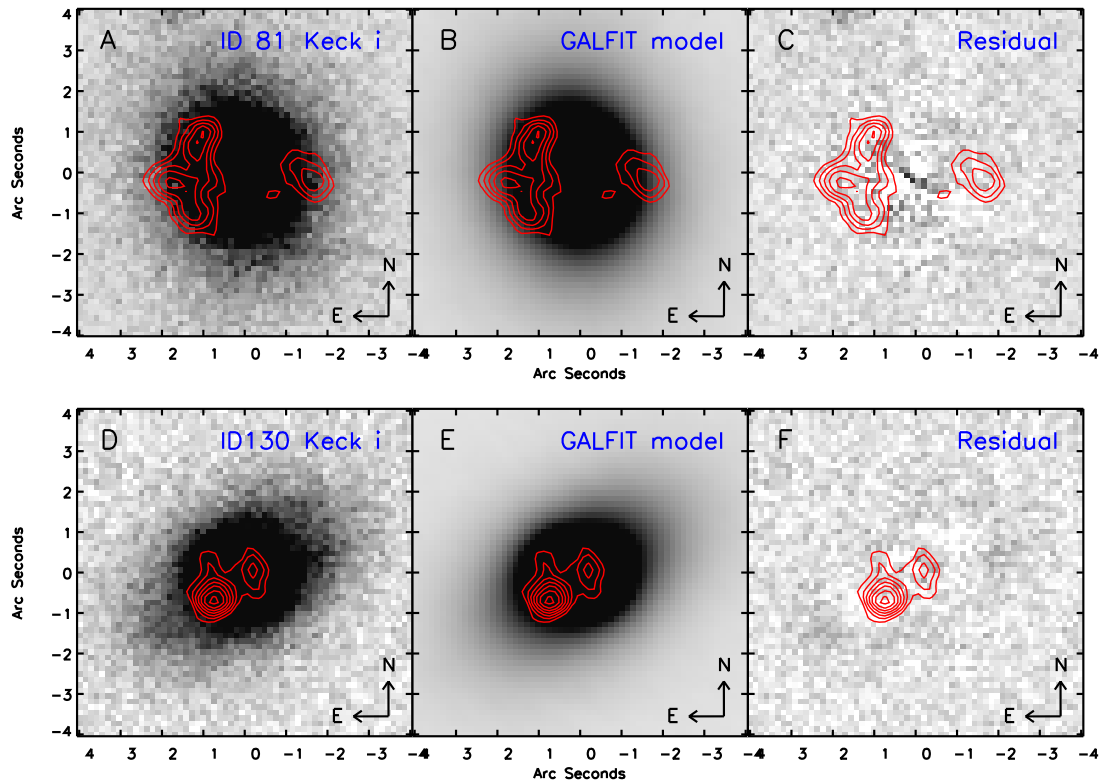
Figure S 7: Decomposition of the best-fit models of the lens galaxies in ID17, ID81 and ID130. *Top*: ID17 shows two partially superimposed components, indicative of two distinct lens galaxies, each described by a relatively shallow Sersic profile. *Middle*: ID81 has one single lens galaxy whose light profile is reproduced by the sum of a Sersic profile and an exponential disk profile. *Bottom*: ID130 is similar to ID81, with the light profile being described by the superposition of a compact Sersic profile and an exponential disk profile. In both ID81 and ID130, the SMA contours (in red) are overlaid on the optical images, in steps of 6σ, 8σ, 10σ, etc.
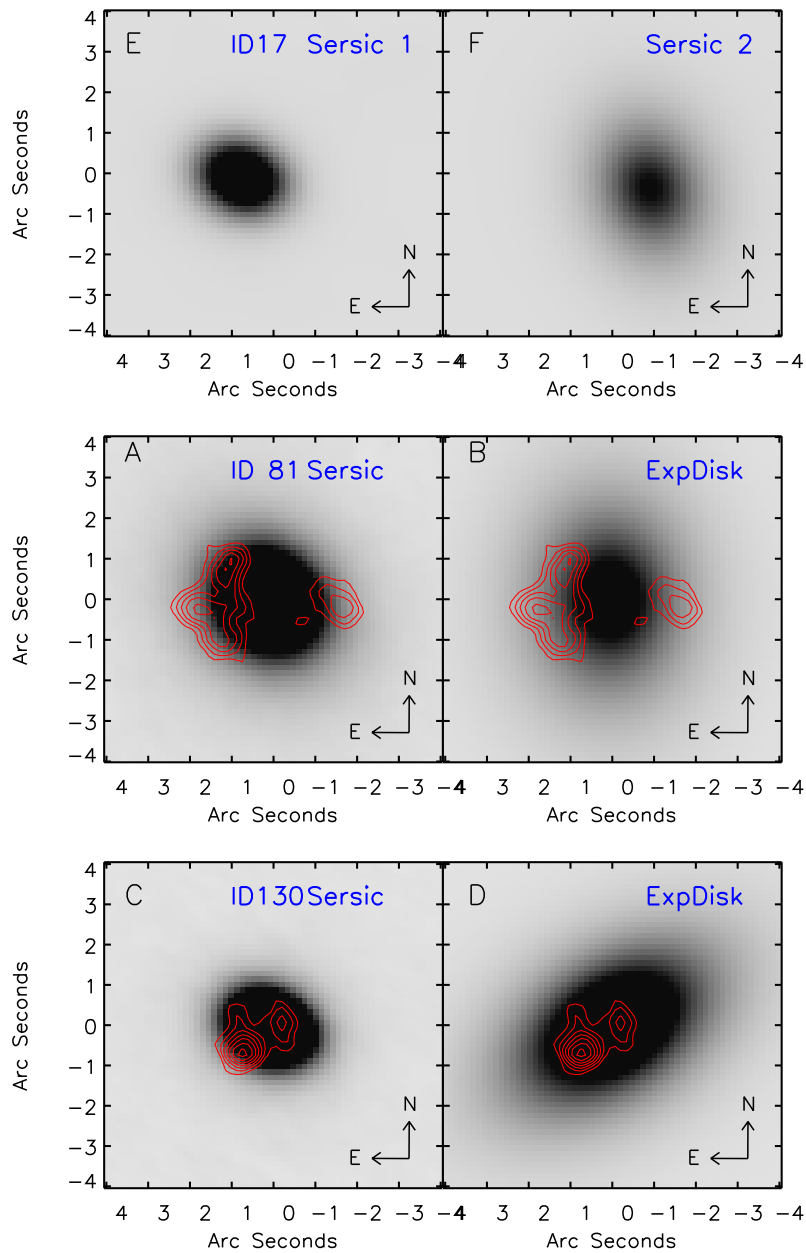
Figure S 8: Light profile of the lens galaxy in the gravitational lens systems ID81 and ID130. In both cases the best-fit to the observed light distribution of the lens galaxy is achieved using 2 components, i.e. an inner (more compact) Sersic profile and an exponential disk profile. These components are shown as a function of the distance from the galaxy center for ID81 (left-hand panel) and ID130 (right-hand panel).
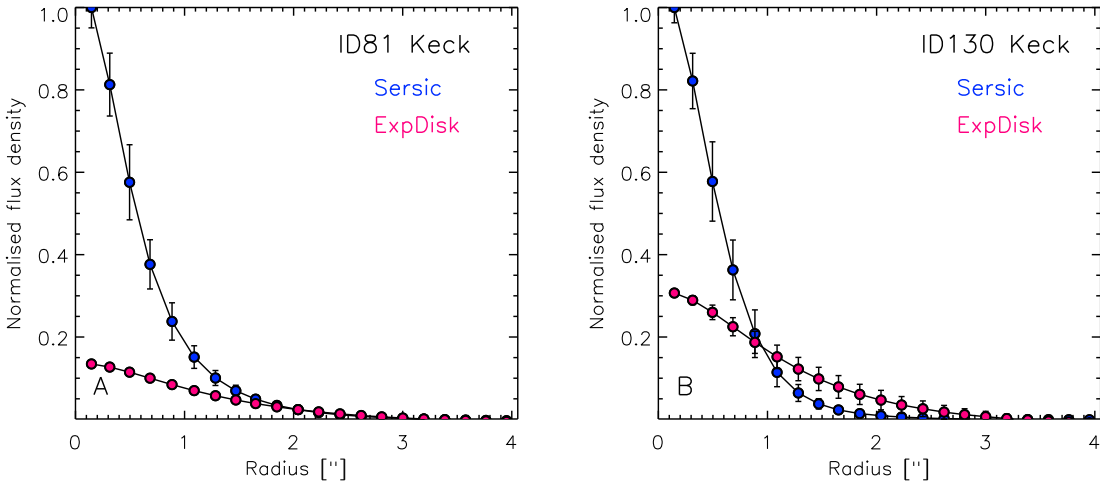
Figure S 9: Lens modelling of ID81 and ID130. The LENSMODEL software was used to fit the position of the peaks in the SMA images. A SIE model was assumed for the mass distribution of the foreground lenses. The image positions used in the fit are indicated by the red dots and correspond to the peaks in the SMA images (red contours in steps of 6σ, 8σ, 10σ etc.). The blue stars are the best-fit positions of the lensed background source, assumed to be point-like. The best-fit position of the lens galaxy and of the background source are marked by the yellow and the blue dots, respectively. The caustic lines and critical lines of the best-fit lens model are indicated in green and yellow, respectively, while the yellow dashed line shows the major axis of the mass model. The simulated image shows the lensed image of a background source (after convolution with the SMA point spread function and added noise) described by a Gaussian profile with FWHM$= 0.2''$.
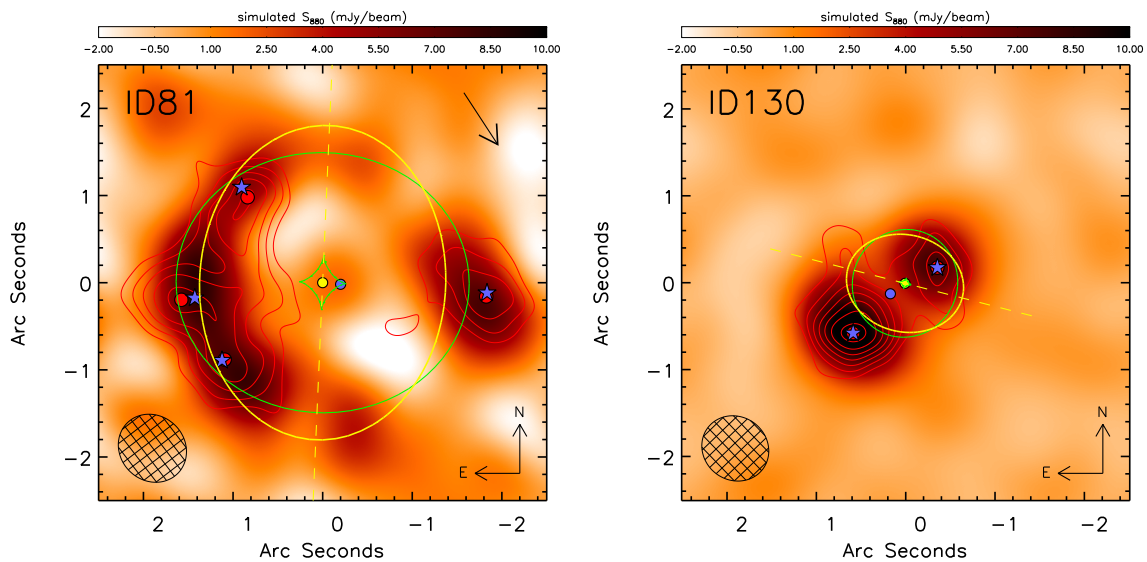
Tables

Table S 1: Submillimeter/millimeter fluxes for the lens candidates. The official H-ATLAS ID, according to IAU (International Astronomical Union) convention, is that derived from the position of the sources in the H-ATLAS SDP catalogue. The quoted errors on the *Herschel* flux densities include statistical errors, confusion noise and an absolute calibration uncertainty of 10 per cent for PACS/100μm, 20 per cent for PACS/160μm and 15 per cent for SPIRE. 3σ upper limits at PACS wavelengths are provided when no detection is achieved at that significance level. Note that ID130 lies just outside the region covered by PACS. Fluxes at 880 μm are from the SMA, while those at 1200 μm are from the MAMBO array at the Institut de Radioastronomie Millimétrique (IRAM) 30 m telescope.

H-ATLAS ID	SDP ID	S_{100} (mJy)	S_{160} (mJy)	S_{250} (mJy)	S_{350} (mJy)	S_{500} (mJy)	S_{880} (mJy)	S_{1200} (mJy)
H-ATLAS J090740.0−004200	9	187±57	416±94	485±73	323±49	175±28	−	7.6±0.8
H-ATLAS J091043.1−000321	11	198±55	397±90	442±67	363±55	238±37	−	12.2±1.2
H-ATLAS J090302.9−014127	17	78±55	182±56	328±50	308±47	220±34	−	15.3±1.3
H-ATLAS J090311.6+003906	81	≤62	≤83	129±20	182±28	166±27	76.4±3.8	20.0±0.7
H-ATLAS J091305.0−005343	130	−	−	105±17	128±20	108±18	39.3±2.3	11.2±1.2

Table S 2: UV/optical/NIR photometry for the lens candidates. UV data are from GALEX, optical photometry is from SDSS and NIR data are from UKIDSS [as reprocessed by GAMA; (*11*)]. Where photometric measurements are not listed it means that the source is not covered at those wavelengths. The 3-σ upper limits shown within parenthesis for the UKIDSS wavelengths are obtained from the residual image after the best-fit GALFIT model of the source has been subtracted off. These limits are used to constrain the SED of the background source.

SDP ID	9	11	17	81	130
GALEX FUV (μJy)	-	-	-	0.23±0.18	-
GALEX NUV (μJy)	-	-	-	1.9±1.1	-
SDSS u (μJy)	0.24±0.23	0.57±0.59	3.3±1.6	3.9±2.0	1.7±1.7
SDSS g (μJy)	1.79±0.43	1.01±0.45	3.9±6.4	24.9±1.1	19.41±0.72
SDSS r (μJy)	5.81±0.70	3.94±0.65	7.7±1.0	114.8±2.1	66.1±1.2
SDSS i (μJy)	14.9±1.1	11.3±1.0	15.3±1.5	197.7±3.6	108.6±2.0
SDSS z (μJy)	27.0±3.7	21.5±4.2	11.8±6.0	278.0±3.6	143.2±6.6
UKIDSS Y (μJy)	-	-	27.7±9.5(<6.6)	321.3±3.2(<6.3)	-
UKIDSS J (μJy)	-	102.4±9.8(<16)	56±17(<12)	367±11(<9.2)	-
UKIDSS H (μJy)	73±15(<5.0)	237±17(<14)	107±19(<8.2)	508.1±5.3(<8.5)	-
UKIDSS K (μJy)	132±24(<6.5)	-	108±23(<9.7)	573.7±6.2(<14)	-

Table S 3: Technical information on the SMA follow-up observations. This includes: the date the measurements were taken (Date), the configuration of the antennas (Conf.; VEX='very-extended', SUB='sub-compact', COM='compact'), the number of antennas used (Nant.), the projected baselines lengths (min/mean/max Pr Baselines), the Local Oscillator Frequency (LO Freq.), and the on−source integration time (Int. time).

SDP ID	Date	Conf.	Nant.	min/mean/max Pr Baselines (m)	LO Freq. (GHz)[a]	Int. time (min)
81	25Feb10	VEX	7	69/281/509	340.7	289
130	28Feb10	VEX	7	76/289/509	340.7	298
81	16Mar10	SUB	5	6/ 17/ 25	340.7	144
130						152
81	09Apr10	COM	6	9/ 38/ 69	341.6	153
130						144

[a]Total bandwidth coverage is LO-8 to LO-4 (LSB) and LO+4 to LO+8 (USB) for a total of 8 GHz. The small difference in LO Frequency between compact configuration observations and the subcompact and very extended observations is not important in this context.

Table S 4: GALFIT results for the five gravitational lens systems. The $3-\sigma$ upper limits given are for an extended source and derived from the distribution of 1.5 arcsecond radius aperture photometry of the Keck maps.

H-ATLAS ID	profile[a]	χ_ν^{2b}	radius[c] (arcsec)	δ^d	Axis ratio	Angle[e] deg.	g-3σ (μJy)	i-3σ (μJy)
9	Sersic	1.07	0.85	5.36	0.72	56.76	0.162	0.641
11	Sersic	1.03	1.10	2.97	0.65	39.61	0.229	0.442
17	Sersic	1.07	0.61	0.54	0.71	63.25	0.202	0.404
	Sersic	–	1.36	0.91	0.69	12.83	–	–
81	Sersic	1.13	0.70	2.82	0.78	36.45	0.130	0.202
	ExpDisk	–	1.20	–	0.72	0.62	–	–
130	Sersic	1.00	0.32	1.23	0.52	56.82	0.198	0.351
	ExpDisk	–	1.11	–	0.55	-54.64	–	–

[a]ExpDisk = exponential disk profile
[b]Reduced χ^2
[c]Radius for Sersic and disk scale length for ExpDisk
[d]Sersic index
[e]Angle measured east of north

References and Notes

1. J. B. Oke, *et al.*, *Publ. Astron. Soc. Pac.* **107**, 375 (1995).

2. J. K. McCarthy, *et al.*, *Society of Photo-Optical Instrumentation Engineers (SPIE) Conference*, S. D'Odorico, ed. (1998), vol. 3355, pp. 81-92

3. S. Guilloteau, *et al.*, *Astron. & Astrophys.* **262**, 624 (1992)

4. http://www.apo.nmsu.edu/arc35m/Instruments/DIS/

5. C. Y. Peng, L. C. Ho, C. D. Impey, H. Rix, *Astron. J.* **124**, 266 (2002)

6. J. J. Condon, *Publ. Astron. Soc. Pac.* **109**, 166 (1997)

7. R. J. Ivison, *et al.*, *Mon. Not. R. Astron. Soc.* **380**, 199 (2007)

8. R. Kormann, P. Schneider, M. Bartelmann, *Astron. & Astrophys.* **284**, 285 (1994)

9. C. R. Keeton, *available at http://xxx.lanl.gov/abs/astro-ph/0102340 (2001)*

10. A. M. Swinbank, *et al.*, *Nature* **464**, 733 (2010)

11. D. Hill, *et al.*, *available at http://xxx.lanl.gov/abs/astro-ph/1009.0615*